

Design and control of a decoupled two degree of freedom translational parallel micro-positioning stage

Lei-Jie Lai, Guo-Ying Gu, and Li-Min Zhu

Citation: *Rev. Sci. Instrum.* **83**, 045105 (2012); doi: 10.1063/1.3700182

View online: <http://dx.doi.org/10.1063/1.3700182>

View Table of Contents: <http://rsi.aip.org/resource/1/RSINAK/v83/i4>

Published by the [American Institute of Physics](#).

Related Articles

Magnetic navigation system for the precise helical and translational motions of a microrobot in human blood vessels

J. Appl. Phys. **111**, 07E702 (2012)

Robotic reconnaissance platform. I. Spectroscopic instruments with rangefinders

Rev. Sci. Instrum. **82**, 113107 (2011)

Actuation of a robotic fish caudal fin for low reaction torque

Rev. Sci. Instrum. **82**, 075114 (2011)

Precise manipulation of a microrobot in the pulsatile flow of human blood vessels using magnetic navigation system

J. Appl. Phys. **109**, 07B316 (2011)

A tuning fork based wide range mechanical characterization tool with nanorobotic manipulators inside a scanning electron microscope

Rev. Sci. Instrum. **82**, 035116 (2011)

Additional information on *Rev. Sci. Instrum.*

Journal Homepage: <http://rsi.aip.org>

Journal Information: http://rsi.aip.org/about/about_the_journal

Top downloads: http://rsi.aip.org/features/most_downloaded

Information for Authors: <http://rsi.aip.org/authors>

ADVERTISEMENT



HAVE YOU HEARD?

Employers hiring scientists
and engineers trust
physicstodayJOBS



<http://careers.physicstoday.org/post.cfm>

Design and control of a decoupled two degree of freedom translational parallel micro-positioning stage

Lei-Jie Lai, Guo-Ying Gu, and Li-Min Zhu^{a)}

State Key Laboratory of Mechanical System and Vibration, School of Mechanical Engineering, Shanghai Jiao Tong University, Shanghai 200240, China

(Received 12 April 2011; accepted 17 March 2012; published online 5 April 2012)

This paper presents a novel decoupled two degrees of freedom (2-DOF) translational parallel micro-positioning stage. The stage consists of a monolithic compliant mechanism driven by two piezoelectric actuators. The end-effector of the stage is connected to the base by four independent kinematic limbs. Two types of compound flexure module are serially connected to provide 2-DOF for each limb. The compound flexure modules and mirror symmetric distribution of the four limbs significantly reduce the input and output cross couplings and the parasitic motions. Based on the stiffness matrix method, static and dynamic models are constructed and optimal design is performed under certain constraints. The finite element analysis results are then given to validate the design model and a prototype of the XY stage is fabricated for performance tests. Open-loop tests show that maximum static and dynamic cross couplings between the two linear motions are below 0.5% and -45 dB, which are low enough to utilize the single-input-single-out control strategies. Finally, according to the identified dynamic model, an inversion-based feedforward controller in conjunction with a proportional-integral-derivative controller is applied to compensate for the nonlinearities and uncertainties. The experimental results show that good positioning and tracking performances are achieved, which verifies the effectiveness of the proposed mechanism and controller design. The resonant frequencies of the loaded stage at 2 kg and 5 kg are 105 Hz and 68 Hz, respectively. Therefore, the performance of the stage is reasonably good in term of a 200 N load capacity. © 2012 American Institute of Physics. [<http://dx.doi.org/10.1063/1.3700182>]

I. INTRODUCTION

Recently, the important role of micro-/nano-positioning technology in hi-tech applications has emerged, including microelectromechanical system, scanning probe microscopy, ultra-precision machining, optical components manufacturing, and biomedical engineering. Many successful micro-positioning stages have been reported.¹⁻⁵ For example, a XYZ scanning stage is used in an atomic force microscope to produce topographic image of specimens with subnanometer resolution.¹ A micro-positioning XY θ table is used in a submicron lithography system.² For micro-/nano-positioning, flexure hinges are often employed to replace conventional joints due to their advantages of no friction, no backlash, no wear, and compact structure. Besides, compared with the other types of actuators, the piezoelectric actuator (PZT) has ultra-high resolution, fast response, high stiffness, and high push force. For the two reasons, PZT-actuated flexure-based stages are widely adopted for micro-/nano-positioning.^{1,2,6}

Flexure-based 2-DOF translational micro-positioning stages can be classified into serial and parallel structures.^{7,8} The characteristic of the serial structure is that one 1-DOF positioning stage is vertically mounted on the other 1-DOF stage.^{1,9} Although this kind of platform is often commercially used and easy to be manufactured, the serial mechanism has many shortcomings such as cumulative errors, parasitic movements, decreased natural frequencies, different dynamic

characteristics along the two directions, large cross couplings, and bulkiness. Compared with the serial mechanism, the parallel mechanism is increasingly adopted in 2-DOF micro-positioning stages due to its advantages of high load capacity, low inertia, high stiffness, balance, and compactness.¹⁰ A parallel-kinematic micro-positioning XY stage is designed by using parallelogram four-bar linkages.⁶ It has a large work space, high bandwidth, and good linearity. A 2-DOF compliant parallel micromanipulator utilizing flexure joints is proposed for two-dimensional nanomanipulation.¹¹ A compliant mechanism consisting of quad-symmetric simple parallel linear springs and quad-symmetric double compound linear springs is proposed for two axes ultra-precision linear motion.⁷ A linear parallel compliant XY-stage based on 4-PP flexure joint mechanism is proposed for ultra-precision motion.¹² Some other XY stages with parallel structure are also reported.^{13,14}

However, most of the stages mentioned above have the cross couplings between the X and Y axes. Cross couplings refer to any motions along the Y direction in response to an actuation along the X direction, and vice versa. The decoupled function, which means that one actuator produces only one axial output motion of the end-effector, is an important performance requirement of a parallel kinematic XY flexure mechanism.⁸ If the 2-DOF are coupled, an additional calibration step is necessary to determine the transformation matrix between the actuator coordinates and the motion stage coordinates. Another important challenge in parallel mechanism design is input decoupling, also known as actuator isolation. An

^{a)}Electronic mail: zhulm@sjtu.edu.cn.

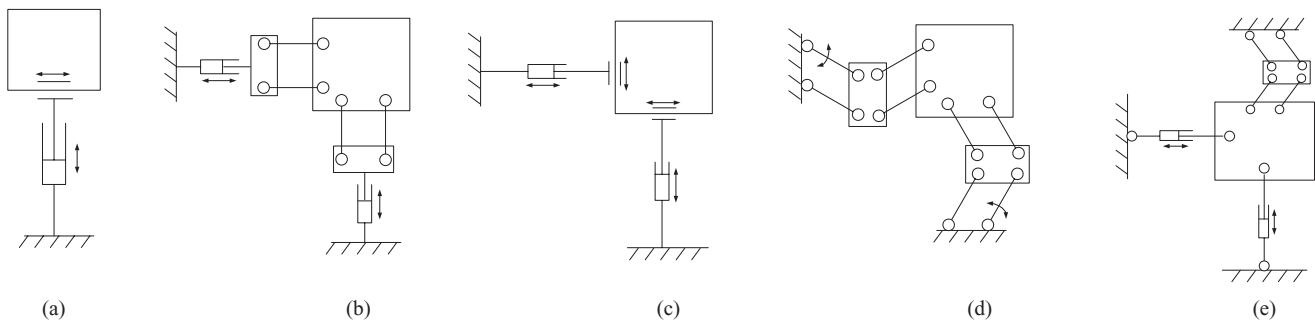


FIG. 1. The possible candidates for 2-DOF translational micro-positioning.

actuator isolation⁸ means that the PZT has to be connected to the point of actuation with little transverse motion in response to any other actuators in the system because the PZT cannot suffer from the transverse load and displacement. To overcome these problems, a constraint-based decoupled parallel kinematic XY flexure mechanism is first proposed.⁸ Based on this conceptual design, a novel flexure-based XY parallel micromanipulator with both input and output decoupling and displacement amplifiers is then proposed.¹⁰ The presented XY stage possesses a mirror-symmetric structure to improve the accuracy performance, and all the prismatic joints are implemented with double compound parallelogram flexures to possess the fully decoupled output motions without crosstalk between the two axes in theory.

This paper presents a novel decoupled parallel micro-positioning stage for 2-DOF translational ultra-precision positioning and tracking. Two types of distributed-compliance compound flexure modules as ideal prismatic joints and a mirror symmetric structure are employed to reduce the input and output couplings, and the parasitic motions. Different from the commonly used flexure modules,^{7,8,11,15} a novel compound flexure module that can produce both large workspace and small maximum stress is developed in this paper. High stiffness ratio between the transverse and working directions of the flexure module guarantees both the objectives of large workspace and actuator isolation. Besides, an additional decoupler plus the actuator isolation provide double protection to the PZT. Compared with the aforementioned work,⁸ this designed stage in this paper is much simpler. It is ease of manufacturing from the economical point of view. Instead of using the lumped-compliance mechanisms,¹⁰ the distributed-compliance module is utilized in the developed stage. It is more likely to have higher structure stiffness and bandwidth in the two translational motions.¹⁴ The higher structure stiffness in loading directions also increase the load capacity of the stage. The design results well meet all the performance objectives of XY mechanisms.⁸

The remainder of the paper is organized as follows. The conceptual design and working principle of the stage are presented in Sec. II. The stiffness matrix model of the stage using the stiffness matrix method is described in Sec. III. The optimal design and the finite element analysis (FEA) validation are performed in Sec. IV. The experimental setup and tests are conducted in Sec. V. Afterward, Sec. VI presents the controller design process, and the experiments are conducted to

demonstrate the performances of the stage and the effectiveness of the controller. Finally, Sec. VII concludes the paper.

II. STRUCTURAL CONCEPT OF THE STAGE

An XY flexure stage has two translational motions along X and Y axes. Five possible candidates for 2-DOF translational mechanism can be found in the literature,^{1,6,10,11} as shown in Fig. 1. If the prismatic joint is used, a micro-positioning stage with serial architecture (see Fig. 1(a)) is produced simply by adding two 1-DOF stages together, one carried by the other, and each of them is driven by a PZT. However, this architecture does not belong to the family of parallel mechanism and has many shortcomings mentioned in Sec. I. Architecture (b) and (d) show two kinds of parallel structures which have PP^R limbs and $P^R P^R$ limbs, respectively. Here P and P^R denote prismatic and parallelogram joints, respectively. Although the P^R joints can always ensure translational movement of the end-effector and retain a fixed orientation with respect to the base whatsoever the motions of PZT may be, the coupled displacement of the P^R joints in architecture (b) and (d) can produce the undesired output cross coupling between two axes. The inverse and forward kinematics models are very complicated, and the cross coupling may also lead to undesired internal resonances. The architecture (e) which has two RPR limbs and a $P^R P^R$ limb can also generate 2-DOF translational motions in theory, however the cross coupling between the two linear motions still exists in this mechanism, and the configuration is too complex. Comparing with the configurations enumerated above, architecture (c) would be an ideal candidate for a decoupled 2-DOF translational micro-positioning stage. It is totally decoupled as long as 2-PP limbs are used. To find two kinds of ideal prismatic joints is crucial in design of this kind decoupled stage.

Based on the above idea, two kinds of P joints are developed, and the conceptual design of the 2-DOF parallel micro-positioning stage consisting of two PZTs and a monolithic compliant mechanism is illustrated in Fig. 2. The compliant mechanism contains two independent kinematic limbs that connect the end-effector to the fixed base. Each of the limbs has two serially connected DOFs which are provided by two P joints, respectively. The two PP limbs with orthogonal architecture are independently actuated by two PZTs. Two types of compound flexure module, which are shown in Fig. 3, are employed as two P joints and combined to be a PP limb. Flexure

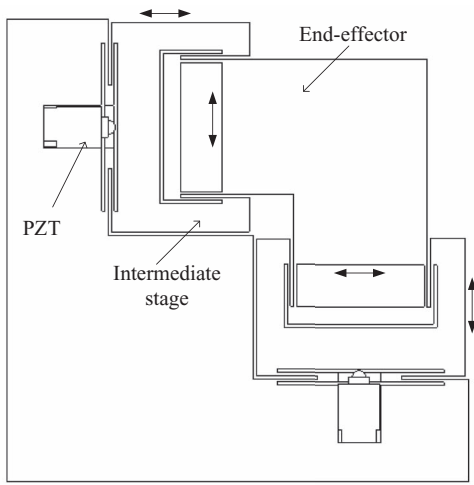


FIG. 2. Design of a XY stage with 2-PP.

module A is the first level flexure module of each limb, which provides 1-DOF. Module A is actuated by the PZT directly and acts as a ideal P joint to realize the pure translational movement for each limb. Flexure module B is the second level flexure module of each limb, which provides the other DOF. Module B adopts the compound double parallelogram flexures to possess fully decoupled output motion without crosstalk between the two axes in theory.¹⁰ The intermediate stage of each limb is connected to the fixed base by means of flexure module A. The end-effector is connected to the intermediate stage via flexure module B. In order to increase the bandwidth and load capacity of the stage, two auxiliary limbs are added to the 2-PP stage, as shown in Fig. 4(a). The symmetrical distribution of the four limbs also provides restriction against any unwanted DOFs of the end-effector. The working principle of the stage is shown in Fig. 4(b).

To show the advantages of the proposed stage, flexure module A and some commonly used flexure modules are used for comparison, as shown in Figs. 3 and 5. When the same forces F_W and F_T are applied to the motion stage in their working and transverse directions, respectively, and the bend-

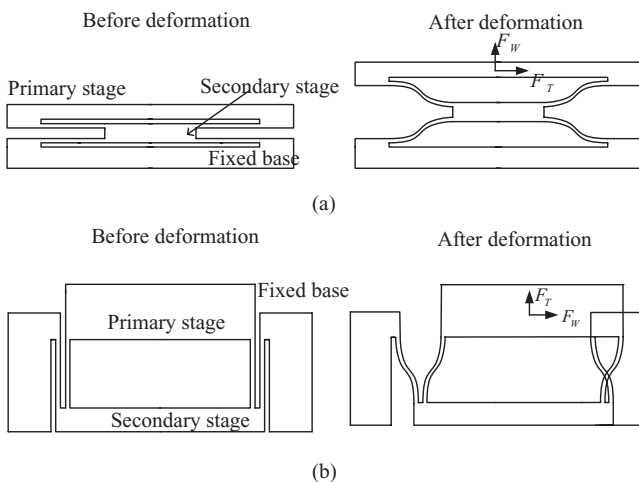


FIG. 3. Compound flexure module. (a) Flexure module A. (b) Flexure module B.

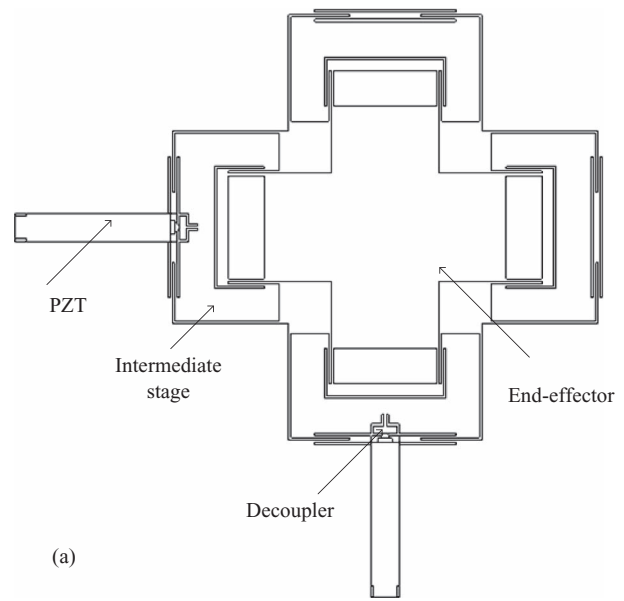


FIG. 4. The 2-DOF parallel micro-positioning stage. (a) Structure of the stage. (b) Working principle of the stage.

ing moments caused by F_T are ignored, the displacements of the four modules have the following relationships:

$$\delta_W^{module A} = 2\delta_W^{DFM} = 4\delta_W^{DPFM} = 2\delta_W^{CDPFM}, \quad (1)$$

$$\delta_T^{module A} = 2\delta_T^{DFM} = 4\delta_T^{DPFM} = 2\delta_T^{CDPFM}, \quad (2)$$

where δ_W and δ_T denote the displacements along the working and transverse directions, respectively. Module A can export the largest displacement, and has a relatively simple shape for the ease of manufacture. Moreover, when the four modules output the same displacement, module A produces the lowest maximum stress at the end of each flexure hinge, the same as

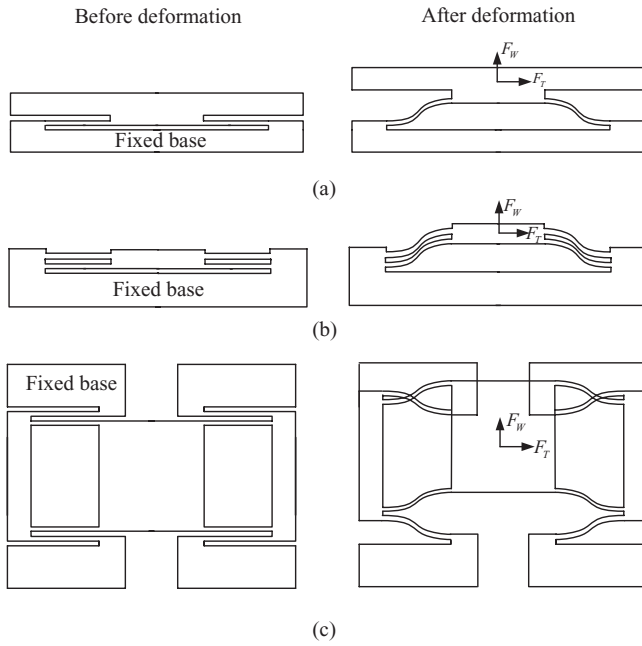


FIG. 5. Commonly used flexure modules. (a) Double flexure module (DFM).¹¹ (b) Double parallelogram flexure module (DPFM).⁴ (c) Compound double parallelogram flexure module (CDPFM).⁷

compound double parallelogram flexure module (CDPFM). As for the stiffness ratio between the stiffness along the transverse and working directions, module A exhibits the same performance as the other modules. Module A has a large transverse stiffness because it is flexible along the working direction and is rigid along the transverse direction. Therefore, it can act as an effective decoupler for its little transverse displacement. Moreover, an decoupler mechanism connecting the PZT and the intermediate stage is used to further avoid damage of the PZT, as shown in Fig. 4(a). The decoupler can transmit the axial force without any loss in motion and absorb any transverse motion without generating transverse loads. Furthermore, the module A and B both adopt the distributed-compliance modules to obtain higher structure stiffness and suppress the vibrations of the the secondary stage.

Due to the use of the compound flexure modules and the mirror symmetric structure, the stage is kinematically decoupled to the maximum extent. The symmetric structure also reduces the parasitic movement; increases the structural stiffness, carrying capacity, and natural frequencies; and exhibits the same static and dynamic performances along the X and Y directions.

III. MODELING THE STAGE USING THE STIFFNESS MATRIX METHOD

For a flexure mechanism, the establishment of the stiffness matrix model is the basic of the static and dynamic analysis. As shown in Fig. 4(b), the total number of rigid bodies in this compliant mechanism is $n = 15$. Denote the 6-DOFs for i th rigid body by $\mathbf{q}_i = [x_i, y_i, z_i, \theta_{xi}, \theta_{yi}, \theta_{zi}]$. Assuming that the mass of the flexures and the elastic deformation of rigid bodies are ignored, all the $6n$ degrees of freedom of the rigid bodies induced in the system are selected as the generalized

coordinates of the system. The displacement vector has the form

$$\mathbf{q} = [\mathbf{q}_1, \mathbf{q}_2, \dots, \mathbf{q}_n]^T. \quad (3)$$

According to the Lagrange's equation, the dynamic differential equation of the system can be represented as

$$\mathbf{M}\ddot{\mathbf{q}} + \mathbf{K}\mathbf{q} = \mathbf{Q}, \quad (4)$$

where the system mass matrix \mathbf{M} is

$$\mathbf{M} = \text{diag}(\mathbf{M}_1, \mathbf{M}_2, \dots, \mathbf{M}_n), \quad (5)$$

the stiffness matrix \mathbf{K} is

$$\mathbf{K} = \begin{bmatrix} \tilde{\mathbf{K}}_{11} & -\tilde{\mathbf{K}}_{12} & \cdots & -\tilde{\mathbf{K}}_{1n} \\ -\tilde{\mathbf{K}}_{21} & \tilde{\mathbf{K}}_{22} & \cdots & -\tilde{\mathbf{K}}_{2n} \\ \vdots & \vdots & \ddots & \vdots \\ -\tilde{\mathbf{K}}_{n1} & -\tilde{\mathbf{K}}_{n2} & \cdots & \tilde{\mathbf{K}}_{nn} \end{bmatrix} \quad (6)$$

and the external force vector \mathbf{Q} is

$$\mathbf{Q} = [\mathbf{Q}_1, \mathbf{Q}_2, \dots, \mathbf{Q}_n]^T. \quad (7)$$

The i th element of the mass matrix \mathbf{M} in Eq. (5) has the form

$$\mathbf{M}_i = \text{diag}(M_{xi}, M_{yi}, M_{zi}, J_{xi}, J_{yi}, J_{zi}), \quad (8)$$

where $(M_{xi} M_{yi} M_{zi})$ denotes the mass of the i th rigid body. J_{xi} , J_{yi} , and J_{zi} are the x , y , and z directional mass inertia moment of the i th rigid body, respectively.

The i th element of the force vector \mathbf{Q} in Eq. (7) is

$$\mathbf{Q}_i = [F_{xi}, F_{yi}, F_{zi}, M_{xi}, M_{yi}, M_{zi}]^T. \quad (9)$$

If only free vibration is considered, \mathbf{Q}_i is set to be 0. A static force-displacement relationship is obtained from Eq. (4) by imposing the acceleration vector $\ddot{\mathbf{q}}$ to be zero. When a force vector \mathbf{Q} is applied, the output displacement vector is

$$\mathbf{q} = \mathbf{K}^{-1}\mathbf{Q}. \quad (10)$$

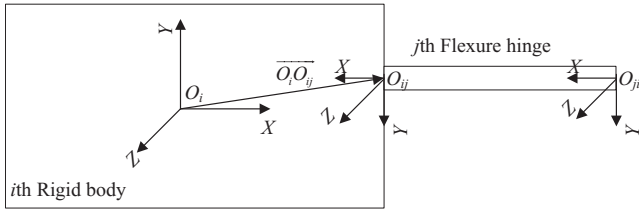
For a general multi-DOF spring-mass system, several methods such as force analysis method, observation method, stiffness and compliance method, and Lagrange equation method are proposed to obtain the stiffness matrix. In this work, the observation method¹⁶ is applied. It is based on the fact that the diagonal element k_{ii} of the stiffness matrix is the sum of the stiffness of the elastic elements connecting with the i th rigid body, and the non-diagonal element is $-k_{ij}$, where k_{ij} is the sum of the stiffness of elastic elements connecting with both the i th and the j th rigid bodies.

Assume that there are n_i flexures connecting with the i th rigid body. As shown in Fig. 6, transforming the displacement screw $\Delta\mathbf{q}_i = [\Delta x_i, \Delta y_i, \Delta z_i, \Delta\theta_{xi}, \Delta\theta_{yi}, \Delta\theta_{zi}]^T$ of the i th rigid body from $O_i - XYZ$ to $O_{ij} - XYZ$ yields

$$\Delta\mathbf{q}_{ij} = \mathbf{J}_{ij}^T \Delta\mathbf{q}_i, \quad j = 1, 2, \dots, n_i, \quad (11)$$

where

$$\mathbf{J}_{ij} = \begin{bmatrix} \mathbf{I} & \mathbf{0} \\ \mathbf{C}(\overrightarrow{O_i O_{ij}}) & \mathbf{I} \end{bmatrix} \begin{bmatrix} \mathbf{R}(O_i/O_{ij}) & \mathbf{0} \\ \mathbf{0} & \mathbf{R}(O_i/O_{ij}) \end{bmatrix}. \quad (12)$$

FIG. 6. i th rigid body connected with j th flexure.

$\mathbf{R}(O_i/O_{ij})$ is the rotation matrix from $O_i - XYZ$ to $O_{ij} - XYZ$. It is characterized by three rotating angles $O_{ij} - XYZ$ with respect to $O_i - XYZ$, and has the form¹⁵

$$\mathbf{R}(\theta) = \mathbf{R}_x(\theta_x) \cdot \mathbf{R}_y(\theta_y) \cdot \mathbf{R}_z(\theta_z), \quad (13)$$

$$\mathbf{R}_x(\theta_x) = \begin{bmatrix} 1 & 0 & 0 \\ 0 & \cos \theta_x & -\sin \theta_x \\ 0 & \sin \theta_x & \cos \theta_x \end{bmatrix}, \quad (14)$$

$$\mathbf{R}_y(\theta_y) = \begin{bmatrix} \cos \theta_y & 0 & \sin \theta_y \\ 0 & 1 & 0 \\ -\sin \theta_y & 0 & \cos \theta_y \end{bmatrix}, \quad (15)$$

$$\mathbf{R}_z(\theta_z) = \begin{bmatrix} \cos \theta_z & -\sin \theta_z & 0 \\ \sin \theta_z & \cos \theta_z & 0 \\ 0 & 0 & 1 \end{bmatrix}, \quad (16)$$

and the matrix $\mathbf{C}(\overrightarrow{O_i O_{ij}})$ is

$$\mathbf{C}(\overrightarrow{O_i O_{ij}}) = \begin{bmatrix} 0 & -r_z & r_y \\ r_z & 0 & -r_x \\ -r_y & r_x & 0 \end{bmatrix}, \quad (17)$$

where $[r_x, r_y, r_z]^T$ represents the vector $\mathbf{r}(\overrightarrow{O_i O_{ij}})$ expressed in $O_i - XYZ$. When $O_i - XYZ$ has a rotational displacement $\Delta\phi_i = [\Delta\theta_{xi}, \Delta\theta_{yi}, \Delta\theta_{zi}]^T$, O_{ij} has an offset translational displacement

$$\mathbf{dr}(\overrightarrow{O_i O_{ij}}) = \Delta\phi_i \times \mathbf{r}(\overrightarrow{O_i O_{ij}}) = \mathbf{C}(\overrightarrow{O_i O_{ij}})^T \Delta\phi_i. \quad (18)$$

As illustrated in Fig. 7, the 6×6 compliance and stiffness matrices of a single straight flexure hinge in its local coordi-

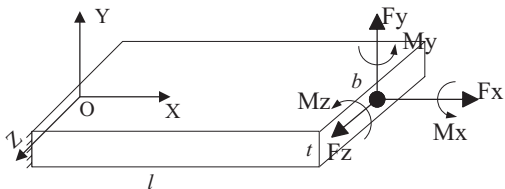


FIG. 7. Model of a flexure hinge.

nate system are described as¹⁷

$$\mathbf{C}^0 = \begin{bmatrix} \frac{l}{Ebt} & 0 & 0 & 0 & 0 & 0 \\ 0 & \frac{4l^3}{Ebt^3} + \frac{l}{Gbt} & 0 & 0 & 0 & \frac{6l^2}{Ebt^3} \\ 0 & 0 & \frac{4l^3}{Ebt^3} + \frac{l}{Gbt} & 0 & -\frac{6l^2}{Ebt^3} & 0 \\ 0 & 0 & 0 & \frac{3l}{Gbt^3} & 0 & 0 \\ 0 & 0 & -\frac{6l^2}{Ebt^3} & 0 & \frac{12l}{Eb^3t} & 0 \\ 0 & \frac{6l^2}{Ebt^3} & 0 & 0 & 0 & \frac{12l}{Ebt^3} \end{bmatrix}, \quad (19)$$

$$\mathbf{K}^0 = (\mathbf{C}^0)^{-1},$$

where E is the elastic modulus, and G is the shear modulus of the material. The stiffness matrix of the flexure hinge is the inverse of the compliance matrix.

Assuming that the stiffness of the flexure represented in $O_{ij} - XYZ$ is \mathbf{K}_{ji} , the force screw applied to point O_{ij} is

$$\mathbf{F}_{ij} = \mathbf{K}_{ji} \Delta\mathbf{q}_{ij} = \mathbf{K}_{ji} \mathbf{J}_{ij}^T \Delta\mathbf{q}_i. \quad (20)$$

When a force vector $\mathbf{f}_{ij} = [f_{x_{ij}}, f_{y_{ij}}, f_{z_{ij}}]^T$ is applied to point O_{ij} , the additional moment vector \mathbf{m}_i with respect to $O_i - XYZ$ is

$$\mathbf{m}_i = \mathbf{r}(\overrightarrow{O_i O_{ij}}) \times \mathbf{f}_{ij} = \mathbf{C}(\overrightarrow{O_i O_{ij}}) \mathbf{f}_{ij}. \quad (21)$$

If \mathbf{f}_{ij} is the force component of \mathbf{F}_{ij} , the equivalent force screw \mathbf{F}_i applied to O_i can be represented as

$$\mathbf{F}_i = [\mathbf{f}_i, \mathbf{m}_i]^T = \mathbf{J}_{ij} \mathbf{F}_{ij} = \mathbf{J}_{ij} \mathbf{K}_{ji} \Delta\mathbf{q}_{ij} = \mathbf{J}_{ij} \mathbf{K}_{ji} \mathbf{J}_{ij}^T \Delta\mathbf{q}_i. \quad (22)$$

Thus, the diagonal sub-matrix $\tilde{\mathbf{K}}_{ii}$ has the form

$$\tilde{\mathbf{K}}_{ii} = \sum_{j=1}^{n_i} \mathbf{J}_{ij} \mathbf{K}_{ji} \mathbf{J}_{ij}^T. \quad (23)$$

Assume that there are n_{ij} flexures connecting with both the i th and j th rigid bodies. As shown in Fig. 8, transforming the displacement screw of the j th rigid body $\Delta\mathbf{q}_j$ from $O_i - XYZ$ to $O_{jik} - XYZ$ yields

$$\Delta\mathbf{q}_{jik} = \mathbf{J}_{jik}^T \Delta\mathbf{q}_j, \quad k = 1, 2, \dots, n_{ij}, \quad (24)$$

where

$$\mathbf{J}_{jik} = \begin{bmatrix} \mathbf{I} & \mathbf{0} \\ \mathbf{C}(\overrightarrow{O_j O_{jik}}) & \mathbf{I} \end{bmatrix} \begin{bmatrix} \mathbf{R}(O_j/O_{jik}) & \mathbf{0} \\ \mathbf{0} & \mathbf{R}(O_j/O_{jik}) \end{bmatrix}. \quad (25)$$

The force screw applied to point O_{jik} is

$$\mathbf{F}_{jik} = \mathbf{K}_{ijk} \Delta\mathbf{q}_{jik} = \mathbf{K}_{ijk} \mathbf{J}_{jik}^T \Delta\mathbf{q}_j. \quad (26)$$

Transforming the force screw \mathbf{F}_{jik} to $O_{ijk} - XYZ$ and then to $O_i - XYZ$ results in

$$\begin{aligned} \mathbf{F}_{ik} &= \mathbf{J}_{ijk} \mathbf{F}_{jik} = \mathbf{J}_{ijk} \mathbf{H}_{ijk} \mathbf{F}_{jik} \\ &= \mathbf{J}_{ijk} \mathbf{H}_{ijk} \mathbf{K}_{ijk} \mathbf{J}_{jik}^T \Delta\mathbf{q}_j = \mathbf{J}_{ijk} \mathbf{H}_{ijk} \mathbf{K}_{ijk} \mathbf{J}_{jik}^T \Delta\mathbf{q}_j, \end{aligned} \quad (27)$$

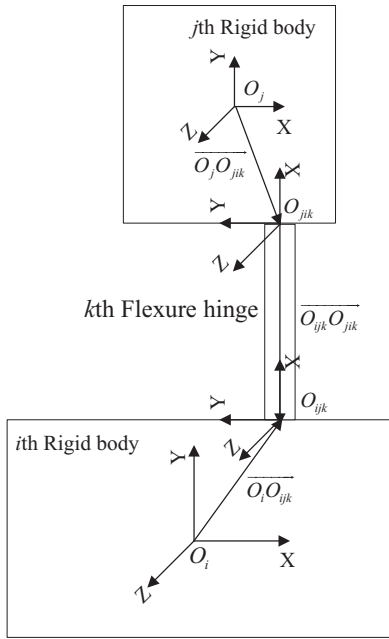


FIG. 8. *i*th rigid body connects with *j*th with *k*th flexure.

where $\mathbf{H}_{ijk} = [\mathbf{c}_{(O_{ijk}/O_{jik})} \quad \mathbf{0}^T]^T$, $\mathbf{J}_{ijk} = [\mathbf{c}_{(O_i/O_{ijk})} \quad \mathbf{0}^T]^T$
 $\times [\mathbf{R}_{(O_i/O_{ijk})} \quad \mathbf{R}_{(O_i/O_{ijk})}^0]$. Hence, the non-diagonal sub-matrix $\tilde{\mathbf{K}}_{ij}$ has the form

$$\tilde{\mathbf{K}}_{ij} = \sum_{k=1}^{n_{ij}} \mathbf{J}_{ijk} \mathbf{H}_{ijk} \mathbf{K}_{ijk} \mathbf{J}_{jik}^T, \quad \tilde{\mathbf{K}}_{ji} = \tilde{\mathbf{K}}_{ij}^T. \quad (28)$$

Considering the first rigid body, there are four parallel flexures connecting to it, as shown in Fig. 9. The diagonal matrix element $\tilde{\mathbf{K}}_{11}$, which is the sum of the stiffness of the four hinges with respect to $O_1 - XYZ$, can be derived as

$$\tilde{\mathbf{K}}_{11} = \sum_{j=1}^4 \mathbf{J}_{1j} \mathbf{K}_{1j} \mathbf{J}_{1j}^T = \sum_{j=1}^4 \mathbf{D}_{1j} \mathbf{R}_{1j} \mathbf{K}_{1j} (\mathbf{D}_{1j} \mathbf{R}_{1j})^T, \quad (29)$$

where

$$\mathbf{D}_{1j} = \begin{bmatrix} \mathbf{I} & \mathbf{0} \\ \mathbf{C}_{(O_1/O_{1j})} & \mathbf{I} \end{bmatrix},$$

$$\mathbf{R}_{11} = \mathbf{R}_{12} = \begin{bmatrix} \mathbf{R}_z(0^\circ) & \mathbf{0} \\ \mathbf{0} & \mathbf{R}_z(0^\circ) \end{bmatrix},$$

$$\mathbf{R}_{13} = \mathbf{R}_{14} = \begin{bmatrix} \mathbf{R}_z(180^\circ) & \mathbf{0} \\ \mathbf{0} & \mathbf{R}_z(180^\circ) \end{bmatrix}.$$

All the sub-matrices of the matrix \mathbf{K} can be obtained from Eqs. (23) and (28). The stage has the same structure in the four limbs; thus, the sub-matrices in the other three limbs can be obtained directly by coordinate transformation. For instance, after coordinate transformation, the diagonal sub-matrices of the 5th, 9th, and 12th rigid bodies illustrated in Fig. 4(b) are obtained as follows:

$$\tilde{\mathbf{K}}_{55} = \begin{bmatrix} \mathbf{R}_z(-90^\circ) & \mathbf{0} \\ \mathbf{0} & \mathbf{R}_z(-90^\circ) \end{bmatrix} \tilde{\mathbf{K}}_{11} \begin{bmatrix} \mathbf{R}_z(-90^\circ) & \mathbf{0} \\ \mathbf{0} & \mathbf{R}_z(-90^\circ) \end{bmatrix}^T,$$

$$\tilde{\mathbf{K}}_{99} = \begin{bmatrix} \mathbf{R}_z(180^\circ) & \mathbf{0} \\ \mathbf{0} & \mathbf{R}_z(180^\circ) \end{bmatrix} \tilde{\mathbf{K}}_{11} \begin{bmatrix} \mathbf{R}_z(180^\circ) & \mathbf{0} \\ \mathbf{0} & \mathbf{R}_z(180^\circ) \end{bmatrix}^T,$$

$$\tilde{\mathbf{K}}_{1212} = \begin{bmatrix} \mathbf{R}_z(90^\circ) & \mathbf{0} \\ \mathbf{0} & \mathbf{R}_z(90^\circ) \end{bmatrix} \tilde{\mathbf{K}}_{11} \begin{bmatrix} \mathbf{R}_z(90^\circ) & \mathbf{0} \\ \mathbf{0} & \mathbf{R}_z(90^\circ) \end{bmatrix}^T. \quad (30)$$

Based on the vibrations theory, the generalized eigenvalues of \mathbf{M} with respect to \mathbf{K} can be obtained by solving the following characteristic equation

$$|\lambda \mathbf{I} - \mathbf{M}^{-1} \mathbf{K}| = 0 \quad (31)$$

and the natural frequencies of the dynamic system described by Eq. (4) are

$$f_i = \frac{1}{2\pi} \sqrt{\lambda_i}, \quad i = 1, 2, \dots, 6n. \quad (32)$$

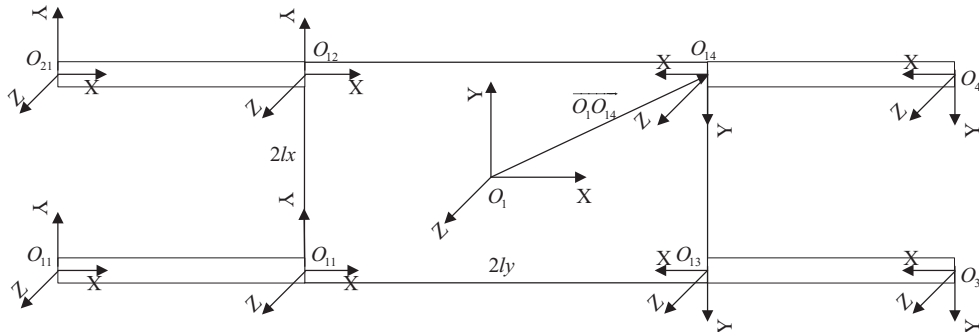


FIG. 9. First rigid body.

TABLE I. Design specifications of the stage.

Travel range	$>40 \times 40 \mu\text{m}$
Unloaded resonant frequency	$> 250 \text{ Hz}$
Maximum driving force	$< 100 \text{ N}$
Load capacity	$> 100 \text{ N}$

IV. OPTIMAL DESIGN AND FEA VALIDATION

A. Optimal design

Optimal design based on the stiffness matrix model described above is performed to obtain the best performance under the design specifications and certain constraints, e.g., the maximum stress should be less than the allowable stress, the workspace should be large enough. Table I illustrates the design specifications of the stage. The objective function of the optimization is the translational natural frequency f of the stage. The variables to be optimized are the dimensional parameters l , b , and t of a single flexure hinge, as shown in Fig. 7. The constraints are described as follows:

- (1) Maximum stress: The maximum stress generated at the root of flexure should be lower than the allowable stress. The constraint can be expressed as

$$\sigma_{\max} = \frac{M}{W} = K \frac{3\delta_{\max} E t}{l^2} \leq [\sigma] = \frac{\sigma_Y}{n}, \quad (33)$$

where M is the maximum bending moment, $W = \frac{1}{6}bt^3$ is the bending section modulus, K is the stress concentration factor, δ_{\max} is the maximum displacement of the

flexure, E is the Young's modulus of the material, σ_Y is the yield stress of the material, and n is the safety factor chosen as 2.5. To reduce the stress concentrations at the root of the flexure, the flexure is designed to be corner-filletted. After finite element analysis over a wide range over different corner radius of the flexures, the stress concentration factor is conservatively specified as 2 corresponded with the zero corner radius.

- (2) Workspace of the stage: The workspace of the stage $\Delta L_s \times \Delta L_s$ should be larger than the threshold determined by the task, which is chosen as $40 \mu\text{m} \times 40 \mu\text{m}$ here. The maximum nominal displacement of the PZT is $\Delta L_{nom} = 45 \mu\text{m}$. The maximum displacement of the stage is

$$\Delta L_s = \frac{K_p \Delta L_{nom} - F_{pre}}{K_s + K_p}, \quad (34)$$

where K_p is the stiffness of the PZT, K_s is the translational stiffness of the stage, and F_{pre} is the preload force which is not considered in the design process of the stage.

- (3) Maximum driving force: Consider that the moving platform may have an acceleration when the PZT tracks sinusoidal or other waveform with high-frequency. The PZT needs to provide the force to generate the acceleration of the stage. The maximum force ($F_{\max} = K_s \Delta L_s$) applied to the stage in the static state is chosen to be less than 1/10 of the PZT's push force capacity which is 1000 N for the selected PZT.

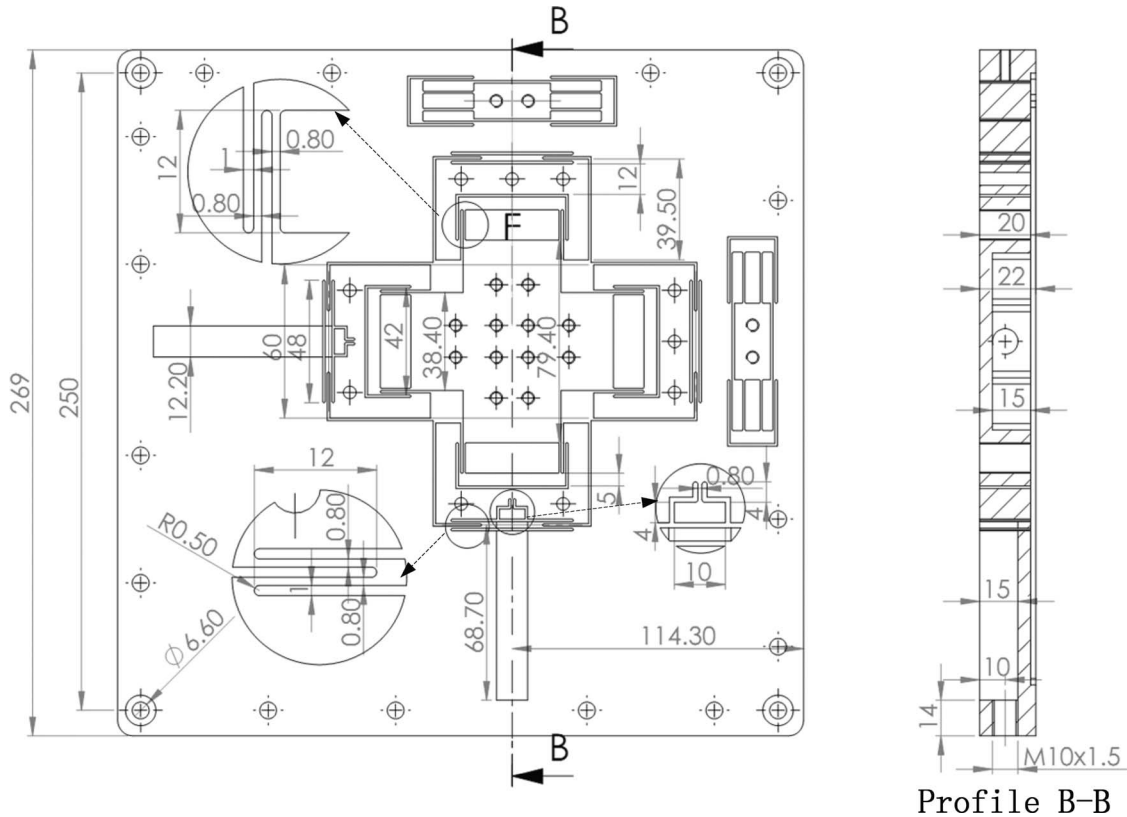


FIG. 10. Dimensional information of the stage.

- (4) Rotational resonance frequency: In order to effectively prevent the rotational movement of the stage, the rotational resonance frequency of the stage is chosen to be two times greater than the translational resonance frequency. Both the translational and rotational resonance frequencies can be calculated from Eq. (32).
- (5) Parameter range: In order to increase the axial stiffness of the flexure hinge and realize the decoupled function provided by flexure module A, the length of the flexure l should satisfy $l \geq 15t$. The ranges of the variables are chosen as follows: $8 \text{ mm} \leq l \leq 20 \text{ mm}$, $18 \text{ mm} \leq b \leq 25 \text{ mm}$, and $0.6 \text{ mm} \leq t \leq 1.5 \text{ mm}$.

The optimization is implemented by the “fmincon” function in MATLAB, and the optimal solutions are $l = 12 \text{ mm}$, $b = 20 \text{ mm}$ and $t = 0.8 \text{ mm}$. Moreover, because the width of the wire cutting path is 1 mm , the corner radius of the flexures is specified as 0.5 mm to reduce the stress concentrations. The detailed dimensional information of the stage are shown in Fig. 10, where all the hinges and limbs are designed with the same dimensions.

Based on the designed parameters of the stage, the motions of the end-effector (the 15th rigid body) are calculated using Eq. (10) when two forces F_x and F_y are vertically applied to the 2nd and 6th rigid bodies. Figure 11(a) shows the calculated displacement of the end-effector along X direction. It is seen that the X directional displacement is independent of the force F_y applied. Figure 11(b) shows the calculated parasitic rotations of the end-effector. It is seen that the rotational parasitic motion does not occur when two equal forces are applied, and increases as the difference between the two directional forces becomes large. However, the rotational parasitic motion is small enough to be ignored. By simplifying the Eq. (10), the planar motions of the end-effector and the two applied forces F_x and F_y have the following relationship:

$$\begin{bmatrix} u_x \\ u_y \\ \theta_z \end{bmatrix} = \begin{bmatrix} 6.06e-7 & -1.10e-38 \\ -1.10e-38 & 6.06e-7 \\ 1.10e-21 & -1.10e-21 \end{bmatrix} \begin{bmatrix} F_x \\ F_y \end{bmatrix}. \quad (35)$$

It is seen that the motions of the stage are decoupled and the parasitic motion is very small.

Considering the load capacity of the stage, when output load vector \mathbf{Q}_{15} is applied to the end-effector, the motions of the end-effector can be calculated by

$$\mathbf{q}_{15} = (\tilde{\mathbf{K}}_{1515})^{-1} \mathbf{Q}_{15}. \quad (36)$$

The non-diagonal elements of the matrix $\tilde{\mathbf{K}}_{1515}$ is much smaller than its diagonal elements. Therefore, the matrix $\tilde{\mathbf{K}}_{1515}$ can be considered as a diagonal matrix, and all the 6-DOFs of the end-effector are decoupled when the external load is applied. The six-axis stiffness of the end-effector derived from the diagonal elements of the $\tilde{\mathbf{K}}_{1515}$ are listed in Table II.

B. FEA validation

In order to verify the optimal design, the finite element analysis (FEA) with ANSYS software is employed to estimate

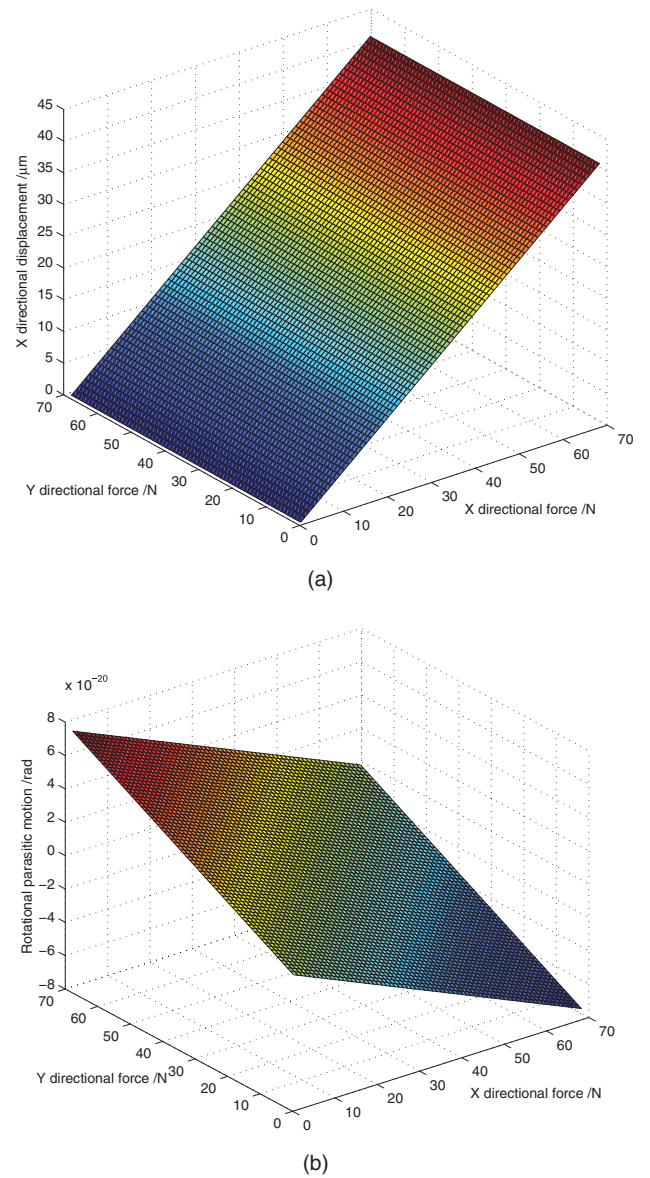


FIG. 11. Displacement of the 15th rigid body. (a) The X directional displacement. (b) Rotational parasitic motion.

the static and dynamic performances of the structure. The three-dimensional (3D) model is generated by Solidworks and subsequently imported to ANSYS in parasolid format. The 3D tetrahedron element SOLID 92 is used to mesh this model. When the designed maximum driving force F_{\max} is applied to the stage and the applied load is zero, the static von-mises stress and deformation are shown in Fig. 12(a). The

TABLE II. Output stiffness of the stage.

K_X	1.626 (N/μm)
K_Y	1.626 (N/μm)
K_Z	10.76 (N/μm)
K_{θ_X}	39.22 (Nm/mrad)
K_{θ_Y}	39.22 (Nm/mrad)
K_{θ_Z}	8.62 (Nm/mrad)

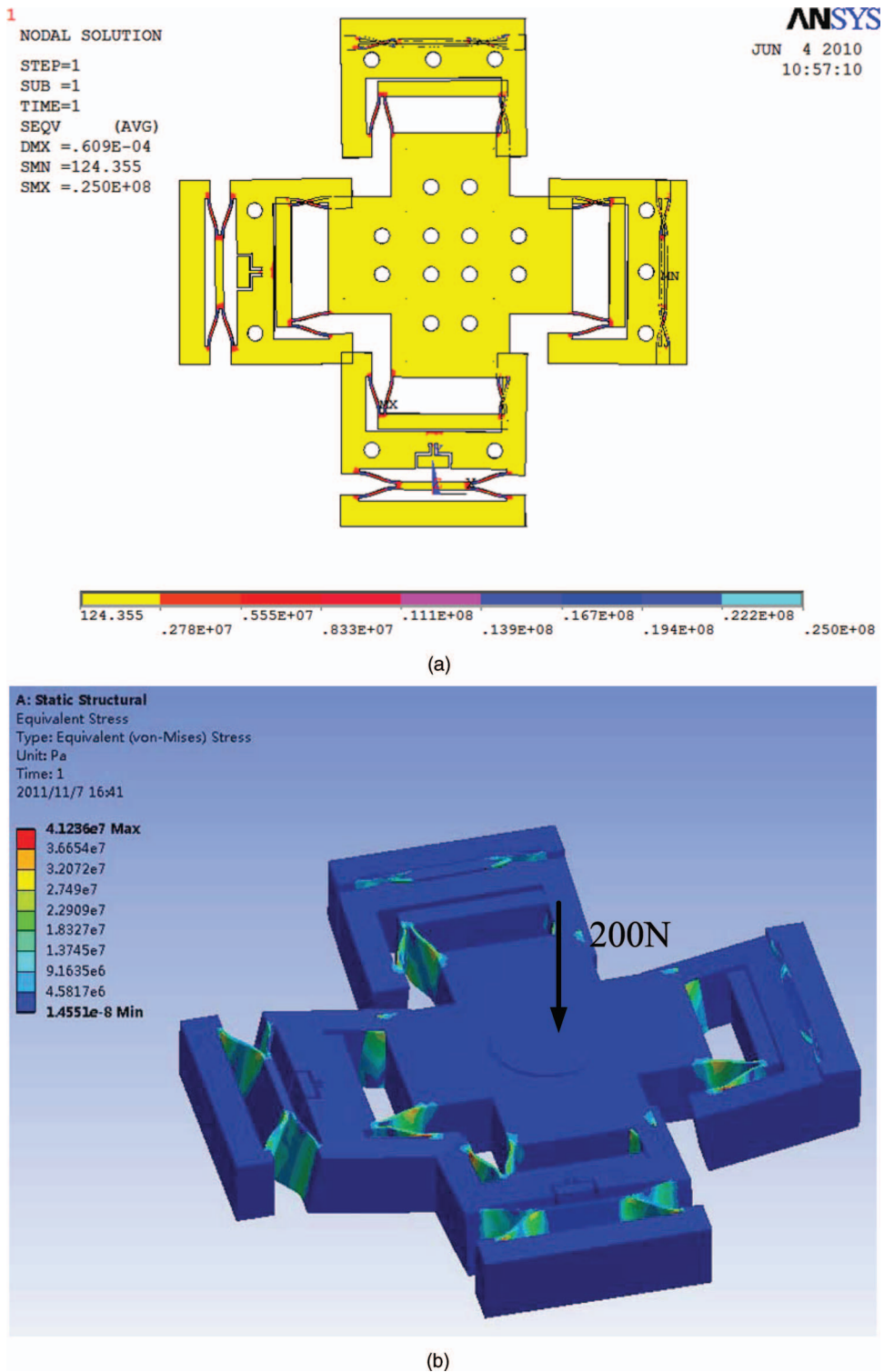


FIG. 12. Static deformation and von-mises stress analyzed by FEA. (a) Static deformation under PZT’s maximum driving force. (b) Von-mises stress under vertical load.

simulation result shows that the stage has a workspace of $41 \mu\text{m} \times 41 \mu\text{m}$ and maximum stress of 25 MPa. Ignoring the stress concentrations, the analytical result of the maximum static stress is calculated as 23 MPa from Eq. (33). It is seen that the maximum stress of the FEA results is 10% larger than the analytical results. Thus the analytical and FEA results can

be in good agreement when the stress concentration factor K is specified as 1.1 for the corner radius of 0.5 mm. Furthermore, Fig. 12(b) shows the von-mises stress distribution when two maximum driving forces and a normal load of 200 N are applied on the stage simultaneously. The maximum stress is only 41 MPa, which is much lower than the allowable stress

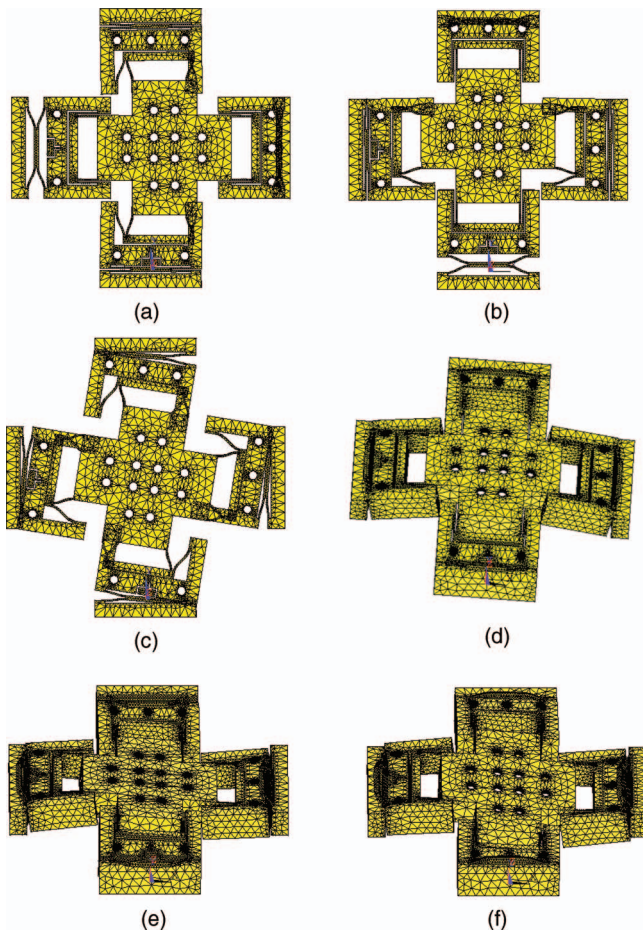


FIG. 13. Modal analysis results provided by FEA.

TABLE III. Comparison of the modal frequencies.

	X- direction	Y- direction	θ_z - direction	Z- direction	θ_x - direction	θ_y - direction
Stiffness matrix (Hz)	417	417	848	982	1604	1604
FEA (Hz)	393	396	842	889	1379	1379
Error	5.17%	5.03%	0.71%	9.47%	14.03%	14.03%

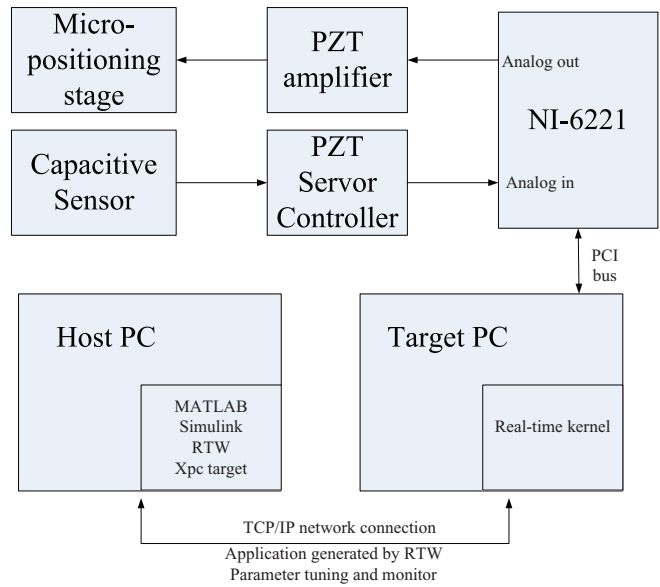


FIG. 15. Block diagram of the whole system.

(200 MPa) of the body material. Therefore, the load capacity of the stage can reach up to 200 N. The modal shapes of the stage are shown in Fig. 13. The unloaded modal frequencies calculated by the stiffness matrix model and the FEA are compared in Table III. The two results agree well. A more specific comparison shows that the resonance vibrations of the secondary stages in the four limbs which are the major sources of the lowest frequency vibrations of the aforementioned mechanism¹⁰ are effectively suppressed due to the use of the distributed-compliance modules. The FEA results also show that the resonant frequencies of the stage at 2 kg and 5 kg load are 128 Hz and 82 Hz, respectively.

V. EXPERIMENTAL SETUP AND TESTS

A. Experimental setup

In this section, an experimental platform as shown in Fig. 14 is established to verify the development. The XY stage is fabricated by wire cutting and the material of the stage is aluminum 7075. Two PZTs (P-840.30 from PI) are adopted to drive the XY stage through a two-channel PZT

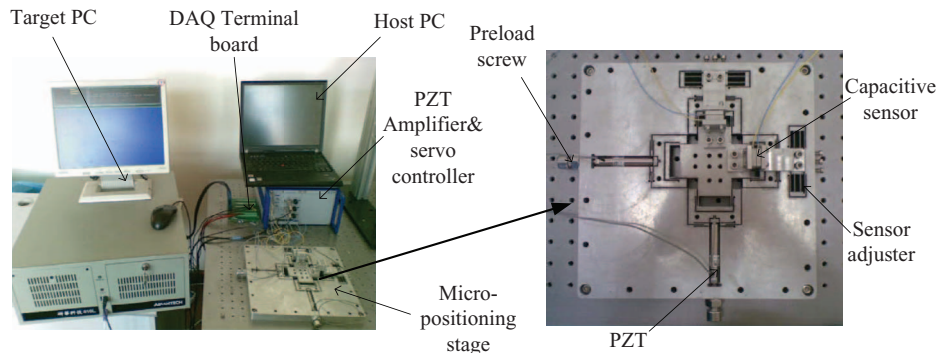


FIG. 14. Experimental setup of the XY micro-positioning stage.

amplifier (E-503.00 from PI). Two capacitive displacement sensors (D-100.00 from PI) are used to measure the displacements along the X and Y directions of the stage. The analog voltage outputs of the two sensors are connected to a two-channel position servo-control module (E-509 from PI). The data acquisition card (NI-6221 from NI) equipped with 16-bit A/D and D/A converters is used to acquire the voltage of the capacitive sensors (0–10 V) and to apply the control voltage (0–10 V) to the PZT amplifier. A real-time digital control system with the hardware in the loop technique is built to perform the semi-physical simulation based on the xPC target. The real time workshop (RTW) toolbox in MATLAB on the host PC generates real time application codes using Simulink models.¹⁸ The block diagram of the whole system is illustrated in Fig. 15.

B. Static and dynamic test

Several experiments are executed to obtain the static and dynamic performances of the stage. In this paper, all the experiments are conducted when there is no external load applied to the stage. According to the experimental tests, the stage has a workspace of $40 \mu\text{m} \times 40 \mu\text{m}$ which corresponds well with the designed objective and the FEA results. The test of the static cross couplings of the two axes is also performed and the results are shown in Fig. 16. It is seen that the maximum cross couplings between the two axes in open-loop are less than 0.5%, which are small enough to be ignored.

To test the natural frequency of the micro-positioning stage, an impulse force is exerted on the input point of the stage by a modal hammer when the PZTs are not mounted on the stage. The time response in direction X is shown in Fig. 17. The unloaded vibration frequency is about 340 Hz, which shows an error of 18% relative to the FEA result. The error may be caused by the mass of the two capacitive sensors and their mounting bracket, manufacturing tolerances,

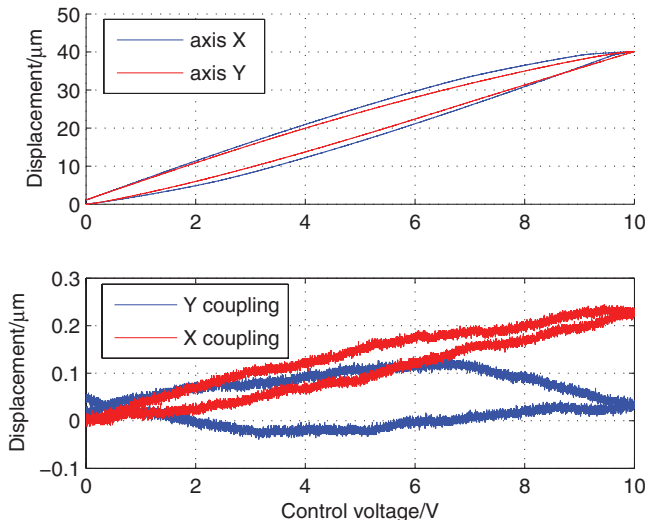


FIG. 16. Experimental results of workspace and coupled displacement.

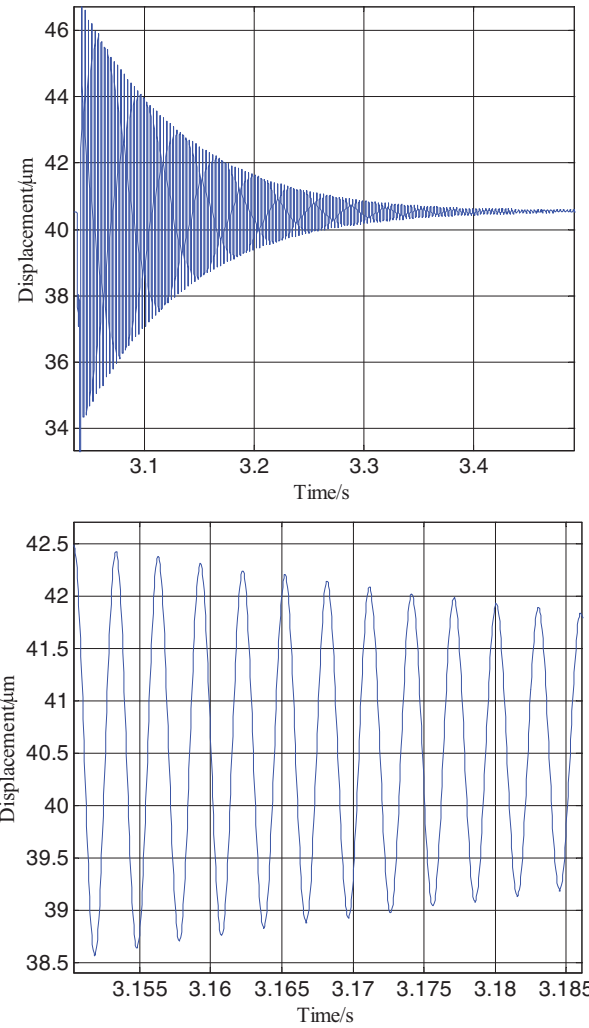


FIG. 17. Time response of force impulse.

and machining imperfections. By the same testing method, the experimental results show that the resonant frequencies of the loaded system at 2 kg and 5 kg are 105 Hz and 68 Hz, respectively. In summary, the loaded resonant frequencies obtained by the stiffness matrix model, the FEA and the tests are listed in Table IV.

To obtain the dynamic characteristic of the whole system, the open-loop step response of the system is analyzed in the time domain. The square wave excitation signals (50 V) are used to drive the PZTs in the X and Y directions, denoted by V_x and V_y (in volts), respectively. The displacement outputs along the X and Y directions of the stage are denoted by D_x and D_y (in μm), respectively. System identification toolbox (*ident*) of MATLAB are used to identify the system models, which are described as $G_{xx} = D_x(s)/V_x(s)$, $G_{yx} = D_y(s)/V_x(s)$, $G_{yy} = D_y(s)/V_y(s)$, and $G_{xy} = D_x(s)/V_y(s)$. The transfer

TABLE IV. Comparison of the loaded resonant frequencies.

	Analytical results (Hz)	FEA results (Hz)	Test results (Hz)
@2 kg	136	128	105
@5 kg	89	82	68

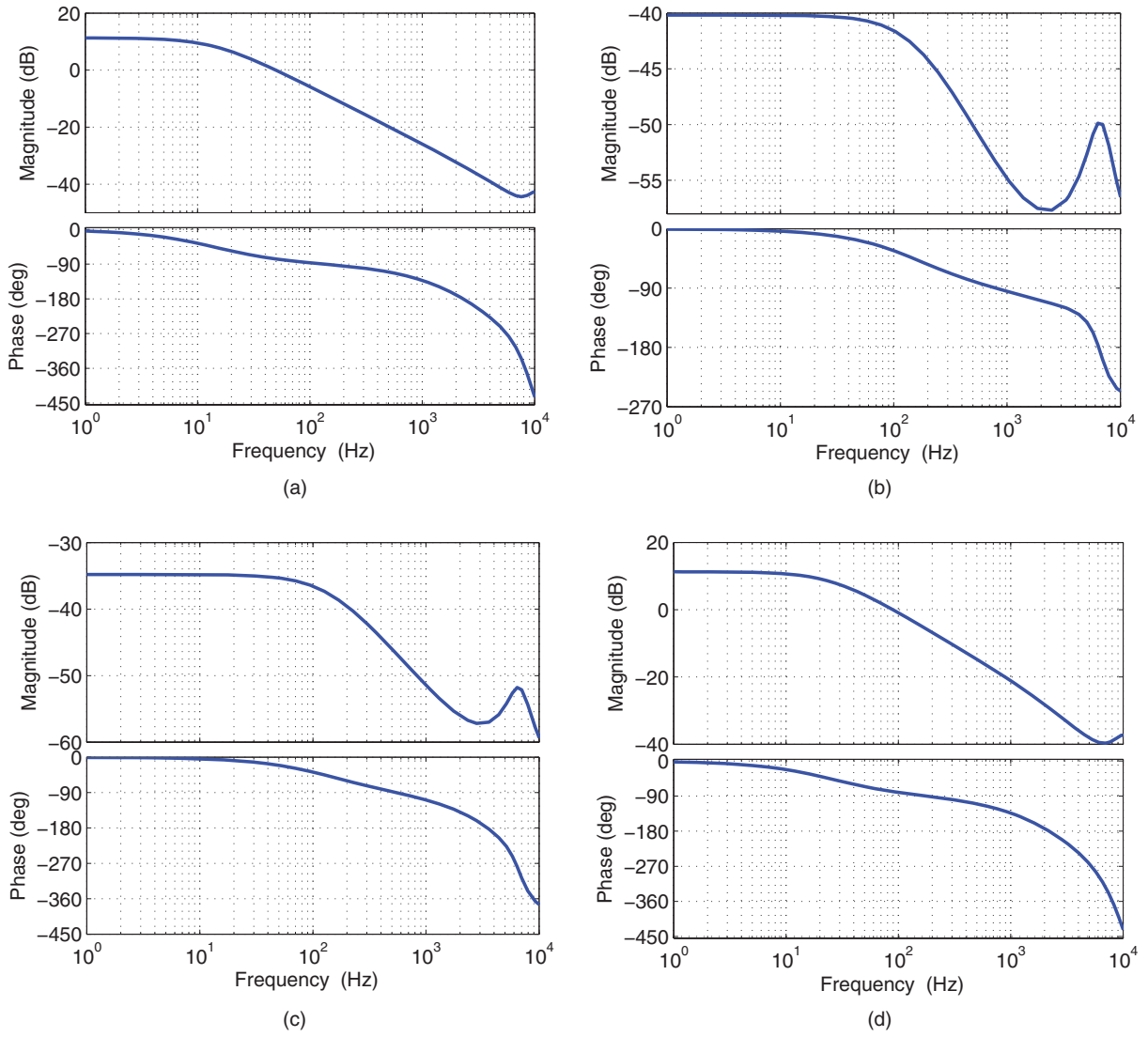


FIG. 18. Frequency response of the identified models. (a) G_{xx} . (b) G_{yx} . (c) G_{xy} . (d) G_{yy} .

functions of the identified models G_{xx} and G_{yy} are given by

$$G_{xx}(s) = \frac{8.01s^3 - 5.932 \times 10^5 s^2 + 4.794 \times 10^{10} s + 1.307 \times 10^{15}}{s^4 + 3.206 \times 10^4 s^3 + 4.279 \times 10^9 s^2 + 2.773 \times 10^{13} s + 3.518 \times 10^{14}}, \quad (37)$$

$$G_{yy}(s) = \frac{-522.1s^3 + 3.847 \times 10^7 s^2 - 1.976 \times 10^{12} s + 3.661 \times 10^{16}}{s^4 + 4.749 \times 10^4 s^3 + 4.701 \times 10^9 s^2 + 6.341 \times 10^{13} s + 9.992 \times 10^{15}}. \quad (38)$$

Figure 18 plots the frequency responses of the identified models G_{xx} , G_{yx} , G_{yy} , and G_{xy} . The magnitude of the cross-coupling terms G_{yx} and G_{xy} are about -50 dB and -45 dB less than that of G_{xx} and G_{yy} , respectively. It is reasonable to utilize single-input-single-out (SISO) control strategies for positioning and tracking control.

VI. CONTROLLER DESIGN AND EXPERIMENTAL RESULTS

A. Controller design

Although the PZT is widely adopted as an actuator in the micro-positioning stage for its excellent features, the

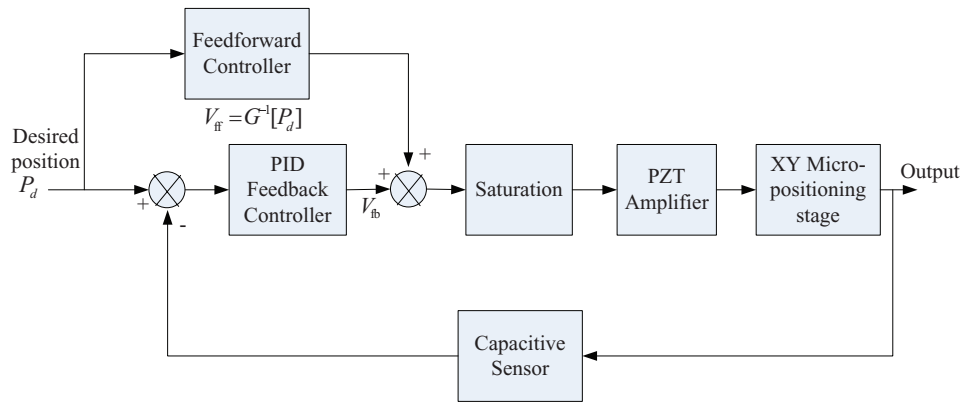


FIG. 19. Block diagram of the implemented control strategy.

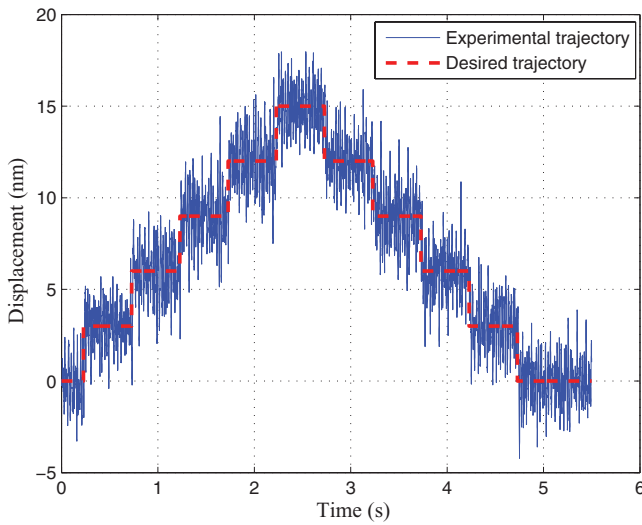


FIG. 20. 3 nm stepwise response.

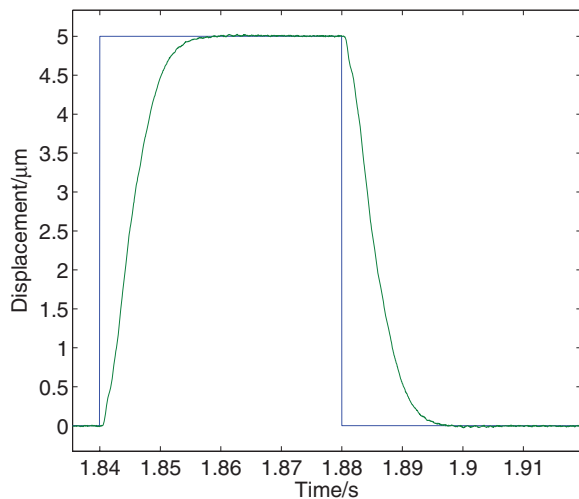


FIG. 21. 5-μm step response of X axis.

performance of the PZT-actuated stage is severely limited by the hysteresis and creep behaviors of the PZT and plant uncertainties of the developed model.¹⁹ In this section, we shall propose a feedback control strategy with an inversion-based feedforward controller.

Based on the developed dynamic model of the stage, an inversion-based control approach is introduced to generate feedforward inputs. For a desired trajectory $P_d(\cdot)$, the feedforward input $V_{ff}(\cdot)$ can be derived by inverting the stage's dynamics G_{xx} and G_{yy} as follows²⁰

$$V_{ff}(\cdot) = G^{-1}[P_d(\cdot)]. \tag{39}$$

Therefore, when the desired trajectory is a periodic sinusoidal of frequency ω , $p_d(t) = a + b \sin(\omega t)$, the inverse feedforward

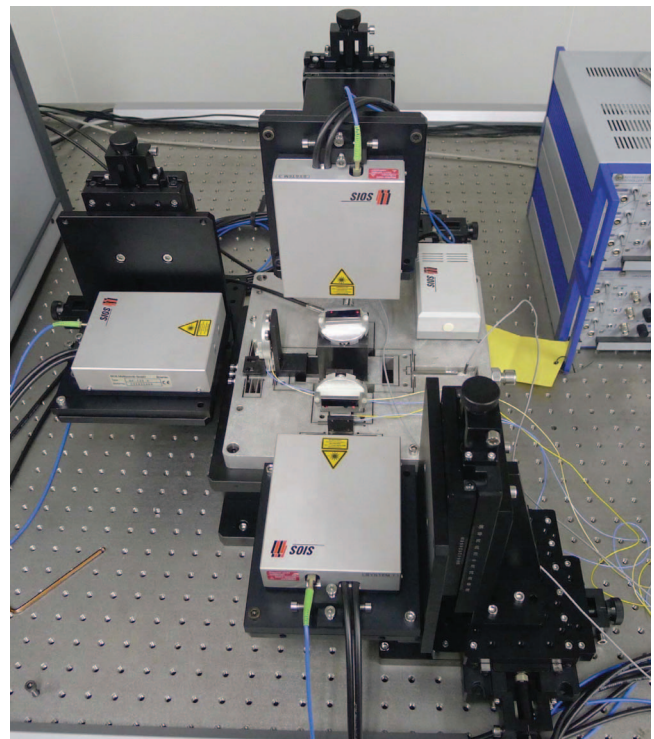


FIG. 22. Multi-dimensional laser interferometer system.

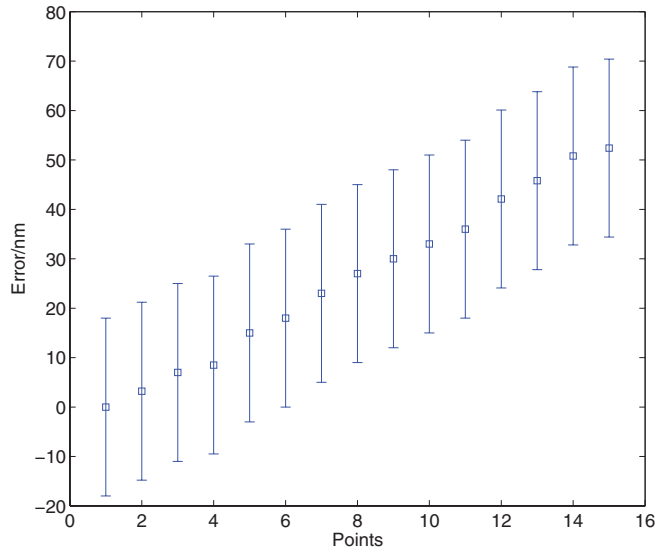


FIG. 23. Repeatability and deviation of the stage.

input can be computed as

$$u_{ff}(t) = \frac{a}{G_{xx}(0)} + \frac{b}{|G_{xx}(i\omega)|} \sin(\omega t - \phi), \quad (40)$$

where $\phi = \angle G_{xx}(i\omega)$. The dc-gain $G_{xx}(0)$ is the ratio of the displacement and voltage for the stage in the static condition. For the periodic triangle trajectory,

$$p_d(t) = B + \sum_{k=1}^{\infty} A_k \sin(\omega_k t), \quad k = 1, 3, 5, 7, 9, \dots, \quad (41)$$

where $A_k = 2A \frac{8}{\pi^2} \frac{(-1)^{(k-1)/2}}{k^2}$, and A is the amplitude of triangular wave. Thus, the feedforward input is

$$u_{ff}(t) = \frac{B}{G_{xx}(0)} + \sum_{k=1}^{\infty} \frac{A_k}{|G_{xx}(i\omega_k)|} \sin(\omega_k t - \phi_k), \quad (42)$$

where $\phi_k = \angle G_{xx}(i\omega_k)$.

Moreover, the traditional proportional-integral-derivative (PID) feedback controller is adopted to compensate for the nonlinearities and uncertainties.²¹ The PID controller in the

TABLE V. Performance specifications and main parameters of the stage.

Travel range	41 × 41 μm
Close-loop positioning resolution	3 nm
Unloaded resonant frequency	340 Hz
Resonance frequency @2kg load	105 Hz
Resonance frequency @5kg load	68 Hz
Stiffness along working direction	1.626 N/μm
Maximum driving force	70 N
Load capacity	200 N
Static/dynamic cross coupling	1.5% / -45 dB
Repeatability	±19 nm
Deviation	50 nm
Yaw/Pitch	4.8/8.4 μrad
Body material	Aluminum7075

TABLE VI. Tracking performance of different controllers at the input rate of 1 Hz and 10 Hz.

Frequency (Hz)	Controller	MTE (μm)	RMSTE (μm)
1	feedback	0.097	0.0024
	feedforward+feedback	0.041	0.000767
10	feedback	0.251	0.074
	feedforward+feedback	0.096	0.021

continuous time domain can be described as

$$u_{fb}(t) = K_p e(t) + K_i \int_0^t e(\tau) d\tau + K_d \frac{de(t)}{dt}, \quad (43)$$

where $e(t) = p_d(t) - p(t)$ is the tracking error with $p(t)$ denoting the actual position measured by the capacitive sensor; K_p , K_i , and K_d are the proportional, integral, and derivative gains, respectively.

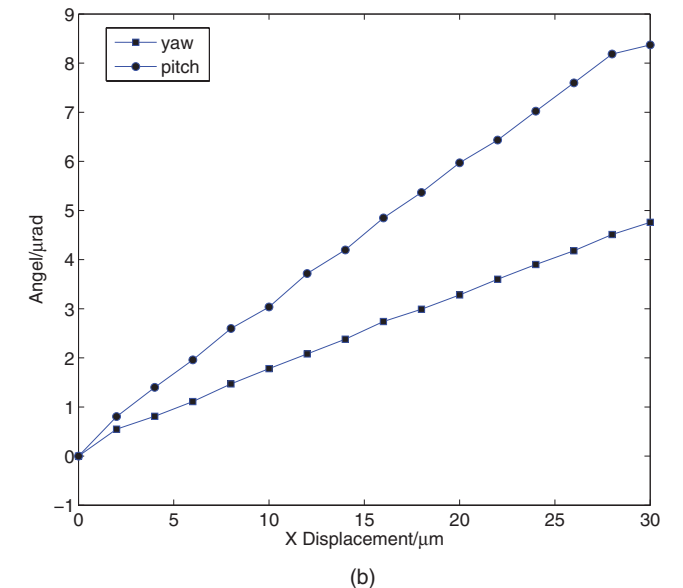
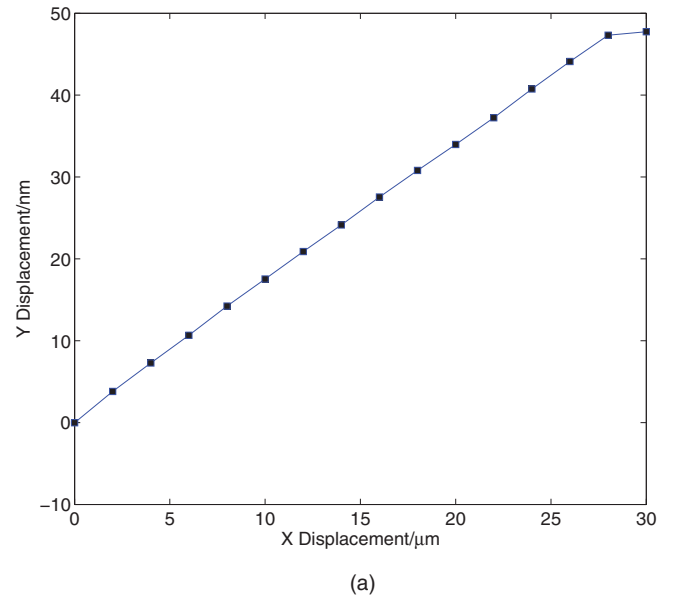


FIG. 24. Coupled displacement and parasitic motions. (a) Cross coupled displacement. (b) yaw and pitch motions.

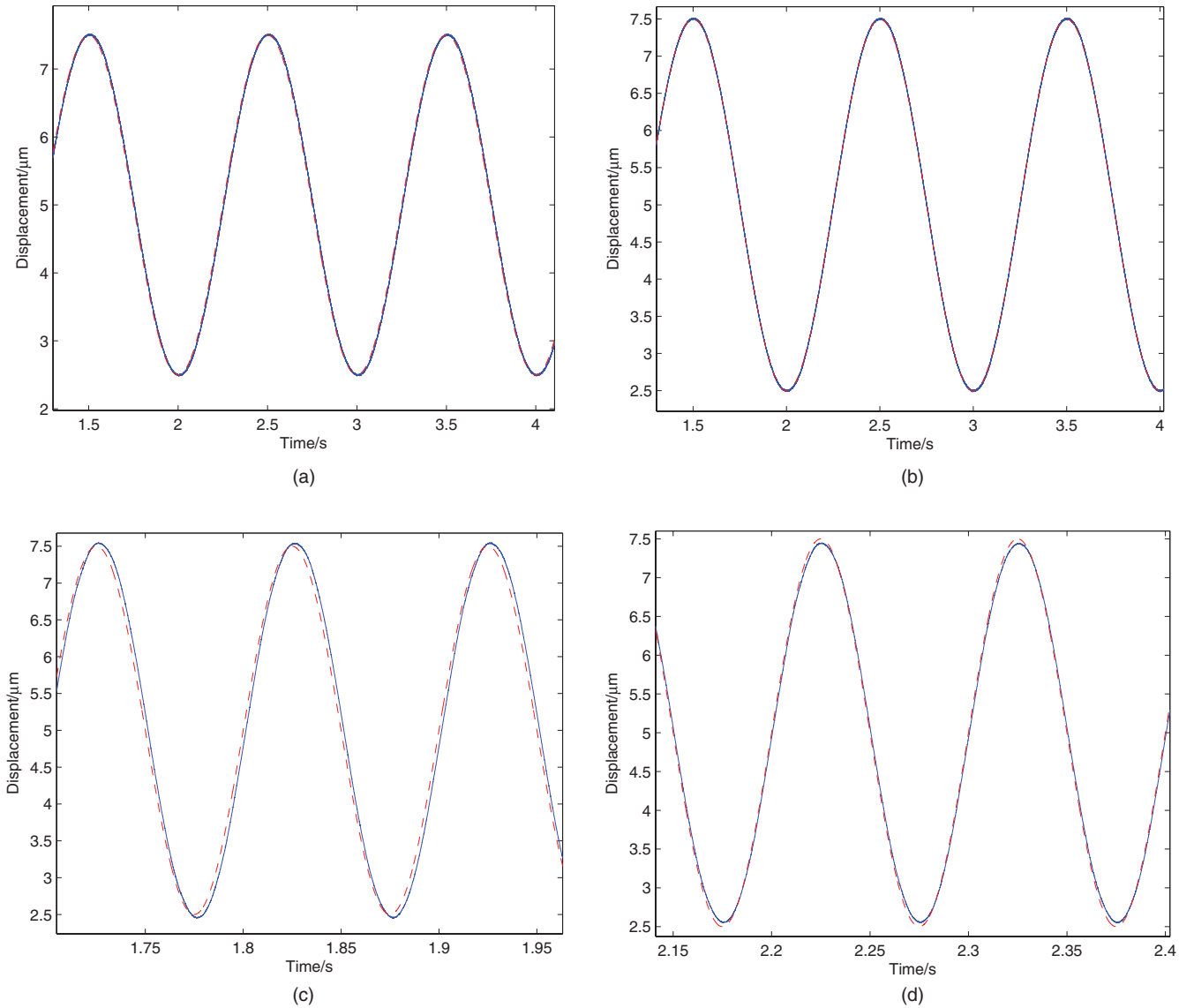


FIG. 25. Experimental results of tracking control. (a) and (c) Tracking performance in feedback control at 1 and 10 Hz, respectively; (b) and (d) tracking performance in feedback and feedforward combined control at 1 and 10 Hz, respectively (dash-reference trajectory, solid-actual trajectory).

For the convenience of a real-time digital control in the xPC target, the discrete form of the PID controller Eq. (43) is implemented in this work. Therefore, the overall control input is derived in a discrete-time form

$$u(kT_s) = u_{ff}(kT_s) + K_p e(kT_s) + K_i \sum_{i=1}^k e(iT_s)T_s + K_d \frac{e(kT_s) - e((k-1)T_s)}{T_s}, \quad (44)$$

where k is the index of the time series and T_s is the sampling time interval ($50 \mu\text{s}$ in this work). Besides, all the computations of $u_{ff}(kT_s)$ in the feedforward controller are performed off-line so as to minimize the execute time to compute the control voltage within a sampling interval. The SISO control block diagram for the XY stage is illustrated in Fig. 19.

B. Experimental results

1. Positioning performance test

To obtain the positioning resolution of the XY stage, an experiment with a staircase input signal with 3 nm height is performed using the PID feedback controller. The PID gains K_p , K_i , and K_d are tuned by trial and error method during the experiments to generate the best control results. In the staircase responses, as shown in Fig. 20, an accuracy of 3 nm is attained. The $5 \mu\text{m}$ step response with PID controller for the stage in X direction is also shown in Fig. 21. The experimental show that the system clearly has fast response (the time constant is less than 15 ms), high resolution, and the low overshoot.

To evaluate the positioning accuracy of the stage, a multidimensional two-beam laser interferometer (SP-120D from SIOS) is employed to measure the six-DOF displacements

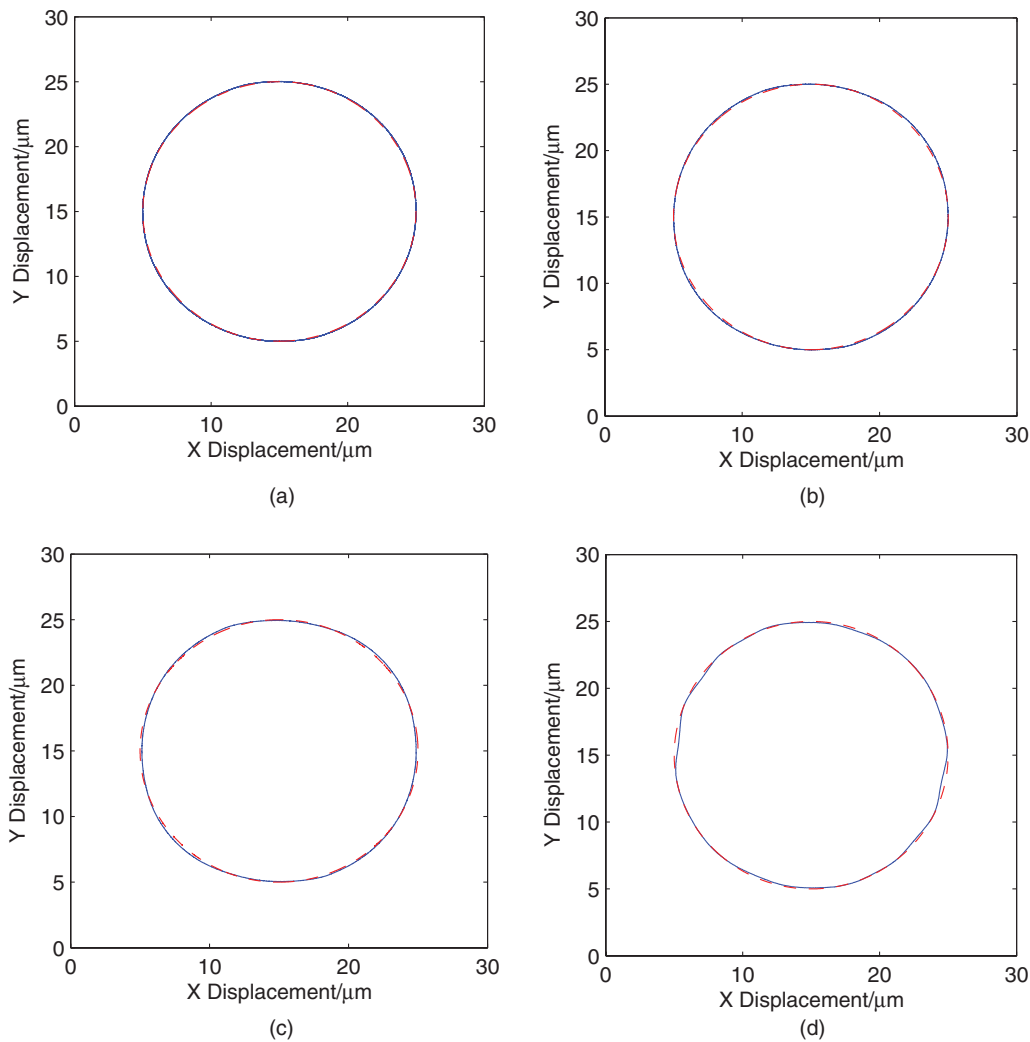


FIG. 26. Circular contouring performance at different velocities. (a) $62.8 \mu\text{m/s}$. (b) $125.6 \mu\text{m/s}$. (c) $251.2 \mu\text{m/s}$. (d) $502.4 \mu\text{m/s}$ (dash-reference trajectory, solid-actual trajectory).

of the end-effector, as shown in Fig. 22. First, the displacements of 15 measurement positions along X axis for $30 \mu\text{m}$ with $2 \mu\text{m}$ steps are measured by laser interferometer back and forth 20 times to determine the linear motion accuracy of the stage. The test results are summarized in Fig. 23. It is seen that the stage has the repeatability of $\pm 19 \text{ nm}$ and the maximum deviation of 50 nm for the travel range of $30 \mu\text{m}$. Secondly, when only the X axis is driven, the displacements in the Y, yaw and pitch directions are measured and the results are depicted in Fig. 24. It is seen that for the $30 \mu\text{m}$ travel range the maximum cross coupling between the two linear motion axes in close-loop is only about 1.5%, and the maximum rotational displacements in the yaw and pitch directions are only about $4.8 \mu\text{rad}$ and $8.4 \mu\text{rad}$, respectively. According to the experiments results, the performance specifications and main parameters of the stage are shown in Table V.

2. Tracking performance test

The tracking performances of the XY stage are evaluated as well. The sinusoidal motion tracking results of the

$5 \mu\text{m}$ peak-to-peak amplitude sine-wave signals at the input frequencies of 1 Hz and 10 Hz are described in Fig. 25. In Table VI, the tracking performance of different controllers is summarized with respect to the maximum tracking error (MTE) and the root-mean-square tracking error (RMSTE).²¹ Compared with the standalone feedback control approach, the feedback plus feedforward control approach reduces the MTE and RMSTE by above 70% when the input frequency is 10 Hz. Tracking accuracy is greatly improved by the developed controller.

The experimental results of circular contouring with a radius of $10 \mu\text{m}$ at four different speeds ranging from $60\text{--}500 \mu\text{m/s}$ are also shown in Fig. 26. No significant distortion of circular motion is shown at high speed. Moreover, the MTE and RMSTE of the circular contouring results are illustrated in the Fig. 27, and they do not increase significantly as the speed increases. The experimental results show that the excellent tracking performance of the stage are achieved by the proposed stage and controller, and the cross coupling between the two linear motions is very small even in the high speed tracking.

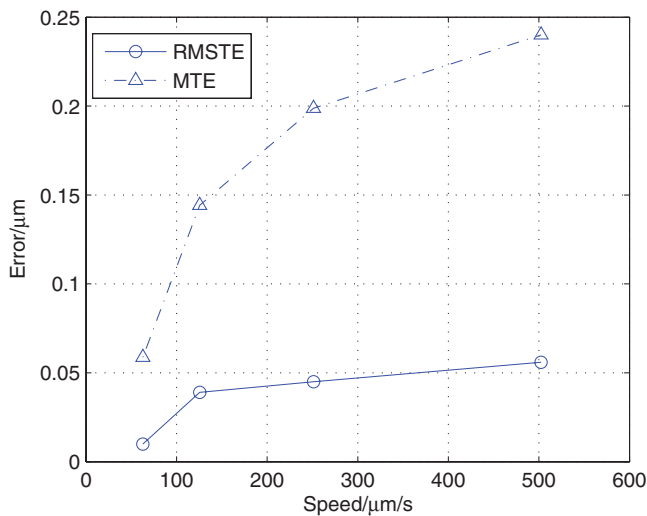


FIG. 27. Circular errors versus speed.

VII. CONCLUSION

In this paper, a decoupled parallel micro-positioning stage is proposed to realize the 2-DOF ultraprecision translational movement. Two types of compound parallel flexure modules and a mirror symmetric structure are utilized to reduce the input and output couplings, and the parasitic motions. The distributed-compliance modules are used to increase the stiffness and bandwidth of the stage. An additional decoupler along with the actuator isolation provides double protection to the PZT. This kind of structure has the advantages of low thermal and manufacturing sensitivity, high structure stiffness, high carrying capacity, and high natural frequency. The stiffness matrix approach is used to model the statics and dynamics of the compliant mechanism, which is validated by FEA via ANSYS. After dimensional optimization, a prototype stage is fabricated by wire cutting. Both the theoretic analysis and experimental tests show good decoupling performance of the stage. Based on the identified dynamic model, an inversion-based feedforward controller in conjunction with a PID controller is applied to compensate for the nonlinearities and uncertainties. The experimental results show that excellent positioning and tracking performances are achieved, which verifies the effectiveness of the proposed

mechanism and controller design. It is worth mentioning that the tested resonant frequencies of the stage at 2 kg and 5 kg load are 105 Hz and 68 Hz respectively, which show very good load capacity of the developed stage. The load capacity can be improved by increasing the minimum thickness (t), thickness (b), and decreasing the length (l) of the flexure. Besides, the layout of stage can be more compact to increase the load capacity.

ACKNOWLEDGMENTS

This work was supported by the National Natural Science Foundation of China (Grant No. 91023047) and the “Shu Guang” project supported by Shanghai Municipal Education Commission (Grant No. 10SG17) and the Science and Technology Commission of Shanghai Municipality (Grant No. 11520701500).

- ¹D. M. Kim, D. W. Kang, J. Y. Shim, I. C. Song, and D. G. Gweon, *Rev. Sci. Instrum.* **76**, 073706 (2005).
- ²K. Sugihara, I. Mori, T. Tojo, C. Ito, C. Tabata, and T. Shinozaki, *Rev. Sci. Instrum.* **60**, 3024 (1989).
- ³B. H. Kang, J. T. Wen, N. G. Dagalakis, and J. J. Gorman, in *Proceedings of the 2004 IEEE International Conference on Robotics & Automation (ICRA '04)*, New Orleans, LA, April 2004, pp. 4097–4102.
- ⁴H. H. Pham and I.-M. Chen, *Precis. Eng.* **29**, 467 (2005).
- ⁵K. X. Hu, J. H. Kim, J. Schmiedeler, and C. H. Menq, *Rev. Sci. Instrum.* **79**, 025105 (2008).
- ⁶Q. Yao, J. Dong, and P. M. Ferreira, *Int. J. Mach. Tools Manuf.* **47**, 946 (2007).
- ⁷K.-B. Choi and D.-H. Kim, *Rev. Sci. Instrum.* **77**, 065106 (2006).
- ⁸S. Awtar and A. H. Slocum, *Trans. ASME, J. Mech. Des.* **129**, 816 (2007).
- ⁹P. Gao, S. M. Swei, and Z. J. Yuan, *Nanotechnology* **10**, 394 (1999).
- ¹⁰Y. M. Li and Q. S. Xu, *IEEE Trans. Rob. Autom.* **25**, 645 (2009).
- ¹¹Y. M. Li and Q. S. Xu, *IEEE Trans. Autom. Sci. Eng.* **3**, 248 (2006).
- ¹²K.-B. Choi and J. J. Lee, in *Proceedings of International Conference on Smart Manufacturing Application (ICSMA 2008)*, Gyeonggi-do, Korea, 9–11 April 2008, pp. 35–38.
- ¹³K. Y. Yuen, S. S. Aphale, and S. O. R. Moheimani, *IEEE Trans. Nanotechnol.* **8**, 46 (2009).
- ¹⁴S. Polit and J. Y. Dong, *J. Manuf. Syst.* **28**, 71–77 (2009).
- ¹⁵L. C. Hale and A. H. Slocum, *Precis. Eng.* **25**, 114 (2001).
- ¹⁶J. W. Ryu, D. G. Gweon, and K. S. Moon, *Precis. Eng.* **21**, 18 (1997).
- ¹⁷K. B. Choi and J. J. Lee, *Rev. Sci. Instrum.* **76**, 075106 (2005).
- ¹⁸P. S. Shiakolas and D. Piyabongkarn, *IEEE Trans. Educ.* **46**, 79 (2003).
- ¹⁹S. S. Aphale, S. S. Devasia, and S. O. R. Moheimani, *Nanotechnology* **19**, 125503 (2008).
- ²⁰G. M. Clayton, S. Tien, K. K. Leang, Q. Z. Zou, and S. Devasia, *ASME, J. Dyn. Syst., Meas., Control* **131**, 061101 (2009).
- ²¹G. Y. Gu and L. M. Zhu, *Rev. Sci. Instrum.* **81**, 085104 (2010).